A new DAS sensor prototype for multicomponent seismic data

Junichi Takekawa[1], Hitoshi Mikada[1], Shibo Xu[1], Masahiro Uno[1,2], Shiori Kamei[1], Kinzo Kishida[2], Daiji Azuma[2], Masafumi Aoyanagi[3], Naoto Tanaka[3], and Hiroki Ichikawa[3]

https://doi.org/10.1190/tle41050338.1

Abstract

We present a novel type of multicomponent sensor prototype that uses distributed acoustic sensing (DAS) technology. A prototype of the new sensor has three individual parts consisting of optical fiber wound around a polyvinyl chloride frame. We deployed the sensor prototype at a test site and recorded seismic waves generated by a wooden hammer. A geophone array was also set for comparison purposes. The data observed with the new DAS sensor prototype show good agreement with the conventional geophone. The particle motion of waveforms obtained by the DAS sensor prototype shows ellipsoidal motion, the propagating velocity of which coincides with the velocity of the Rayleigh waves estimated by the dispersion curve based on the geophone data. We introduced a simple string model to explain the dynamic behavior of the sensor. The analysis results of the string model can explain features of recorded seismic data. These results indicate that the DAS sensor prototype records seismic waves via lateral vibration of the string. The present study shows a new possibility of the multicomponent sensor with the DAS technology.

Introduction

In recent years, seismic data acquisition by way of distributed acoustic sensing (DAS) technology has drawn attention (Mateeva et al., 2013; Hartog et al., 2014; Egorov et al., 2018; Kimura et al., 2018; Luo et al., 2020) because of its advantages over the use of conventional geophones or hydrophones, e.g., dense channels along with an optical fiber and lower cost per channel. The range of its application is extended to monitoring ambient noise (Dou et al., 2017), earthquake engineering (Spica et al., 2020), and earth science (Lindsey et al., 2019). The distributed nature of DAS technology may extend its application to broader study areas. However, DAS must still overcome some challenges to obtain better imaging results in the subsurface than in conventional seismic acquisition.

One of the shortcomings of DAS measurement is that the optical fiber has less sensitivity to seismic waves coming from the broadside. This is known as “broadside insensitivity.” It is essential to record multicomponent data for obtaining better imaging or inversion results in the subsurface (Rusmanugroho and McMechan, 2012; Watanabe et al., 2017). Helically wound optical fiber was proposed to overcome this drawback (Hornman et al., 2013; Kuvshinov, 2016). This type of sensor was designed to have broadside sensitivity and was applied to many fields and numerical experiments (Hornman, 2017; Bakulin et al., 2020; Eaid et al., 2020). Ning and Sava (2018) proposed obtaining all strain tensor components using the least-squares method. Their study examined some configurations with different pitch angles and combinations of helical and straight fibers. The chirping helix configuration was also investigated, and the possibility of reconstruction of the strain tensor was shown apart from challenging tasks for manufacturing and deployment. They assumed that the seismic wavelength was much greater than the analysis window. Furthermore, the estimation of strain tensor requires that the optical fiber is fully coupled to surrounding formations; i.e., the deformation of optical fiber is assumed to be equal to the surrounding strain field induced by incident waves.

The aforementioned approximation does hold in borehole environments. However, coupling an optical fiber and surrounding soil could be a problem in some seismic measurements like near-surface surveys. Innanen et al. (2019) designed and deployed a shaped DAS fiber array for multicomponent sensing. Their study showed the possibility of estimation of strain tensor components. However, some difficulties regarding coverage in the depth direction and the size of the array have remained. Although various trials have been made to develop multicomponent DAS sensors, their development has not been completed yet. Because the study of seismic acquisition with DAS technology has only just begun, the complete acquisition of all wave modes with DAS technology is still challenging. Therefore, many attempts are still required to establish multicomponent DAS sensors.

In Takekawa et al. (2021), a new type of DAS sensor prototype for obtaining multicomponent seismic data was developed. The newly developed sensor has three parts designed to record three-component seismic data, i.e., horizontal and vertical motions. The observed waveforms by the DAS sensor prototype were compared with those of the conventional geophones. The comparison result showed good agreement with each other, and therefore a possibility of a new type of DAS sensor for obtaining multicomponent seismic data was shown. However, the recording mechanism of the DAS sensor prototype has not been fully considered yet. Furthermore, the discussion of the recorded wave mode of each event was also insufficient. In the present study, we consider the recording mechanism of the newly developed DAS sensor prototype and the wave mode of the recorded seismograms.

In the following, we will briefly explain the DAS sensor prototype and configurations of the field experiment. Next, the recorded waveforms by the DAS sensor prototype are compared with those of the conventional geophones. The wave mode of the recorded seismograms is investigated based on particle motion analyses. The recording mechanism of propagating seismic waves is discussed by considering a simple string analysis. Finally, we discuss the possibility of the developed sensor as a multicomponent sensor and future works for industrial applications.

[1]Kyoto University, Kyoto, Japan. E-mail: takekawa@tansa.kumst.kyoto-u.ac.jp; mikada@gakushikai.jp; shibo.xu@tansa.kumst.kyoto-u.ac.jp; kamei211@tansa.kumst.kyoto-u.ac.jp.
[2]Neubrex Co. Ltd., Hyogo, Japan. E-mail: uno@neubrex.jp; kishida@neubrex.jp; azuma@neubrex.jp.
[3]Tadano Ltd., Kagawa, Japan. E-mail: masafumi.aoyanagi@tadano.com; naoto.tanaka@tadano.com; hiroki.ichikawa@tadano.com.

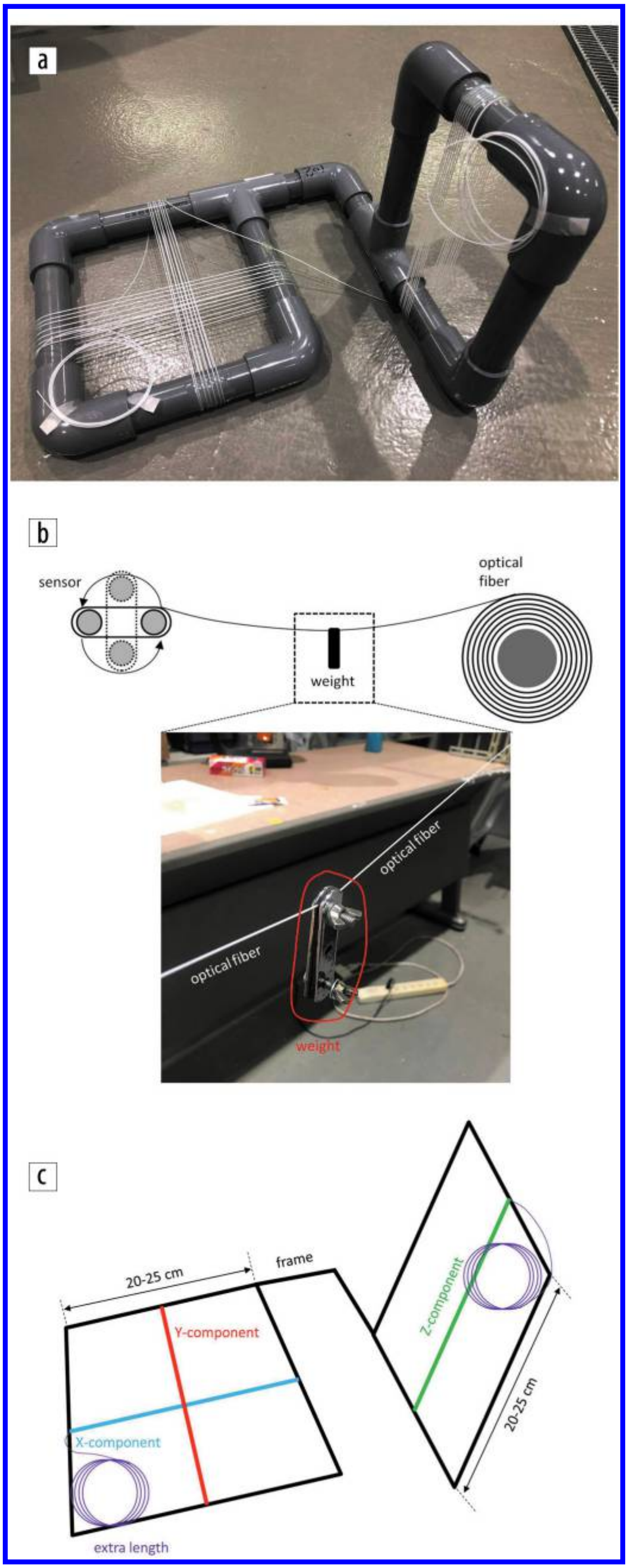

Figure 1. Overview of the developed DAS sensor: (a) photo of the DAS sensor, (b) how to apply the constant tensile force to the optical fiber, and (c) explanation of X-, Y-, and Z-components.

Prototype of new DAS sensor

We developed a prototype of the new DAS sensor. Figure 1a shows an overview of the sensor. We made a frame of polyvinyl chloride parts (cut pipe, elbow, and T-junction), and wound an optical fiber by applying a constant tensile force, as shown in Figure 1b. The tensile force is applied by a weight hung from the string. The frame size is about 20–25 cm, a size chosen to be equivalent to the gauge length of the DAS measurement of about 20 cm. The pipe diameter was 32 mm to minimize the loss of optical power at the winding part. The optical fiber was wound around the same frame seven times (14 turns) for each component. To improve the signal-to-noise ratio (S/N), we take the average of observed waveforms at the free part of the fiber (near the center of the straight part). Contacting parts between the frame and optical fiber are covered with resin to protect the optical fiber against breaking. Therefore, the optical fiber cannot strain at the covered parts, whereas the rest can deform freely. The sensor has three individual parts named X-, Y-, and Z-components, as shown in Figure 1c.

Experimental settings

We deployed the developed DAS sensor prototypes and an array of vertical component geophones in a test field along the survey line. The geophones and the DAS sensor prototypes were placed on the ground and buried in the pits dug down to about 30 cm from the surface. Therefore, the bottom of the DAS sensor prototype was 30 cm below ground level. The geophones recorded the vertical component of the displacement velocity. Figure 2a shows a schematic figure of the experimental settings. We deployed 12 geophones, five buried DAS sensor prototypes, and five surface-placed DAS sensor prototypes. The direction of each axis (x, y, and z) corresponds to the sensor direction in Figure 1c. Figure 2b shows a photo of the test site after deploying geophones and DAS sensor prototypes. Because the purpose of the DAS sensor prototypes on the ground is simply to compare with the sensors in the ground, we put the surface-placed DAS sensor prototypes on the ground without considering the coupling to the ground. On the other hand, the buried DAS sensor prototypes were backfilled by the dip up soil after removing pebbles to achieve good coupling between the optical fiber and the ground. The axial directions of X- and Y-components lay in the horizontal plane, and the Z-component corresponds to the depth direction. All DAS sensor prototypes had extra fiber lengths at the ends of X- and Z-components (Figure 1c). After the deployment, each sensor's ends were fused with the other sensors at the extra part to form a fiber sensor chain. The posterior part of the optical fiber was connected to an extra length of 500 m and bounded by a no-reflection end. A wooden hammer generated the seismic wave. We stacked a total of 20 shot records to improve S/N. The DAS and geophone time sampling intervals were 0.2 ms and 0.1 ms, respectively. DAS measurement was performed by the time-gated digital-optical frequency domain reflectometry (TGD-OFDR) method (Kishida et al., 2020, 2021). The gauge length in this measurement is 0.2 m. Details of the spatial resolution are discussed in the following section.

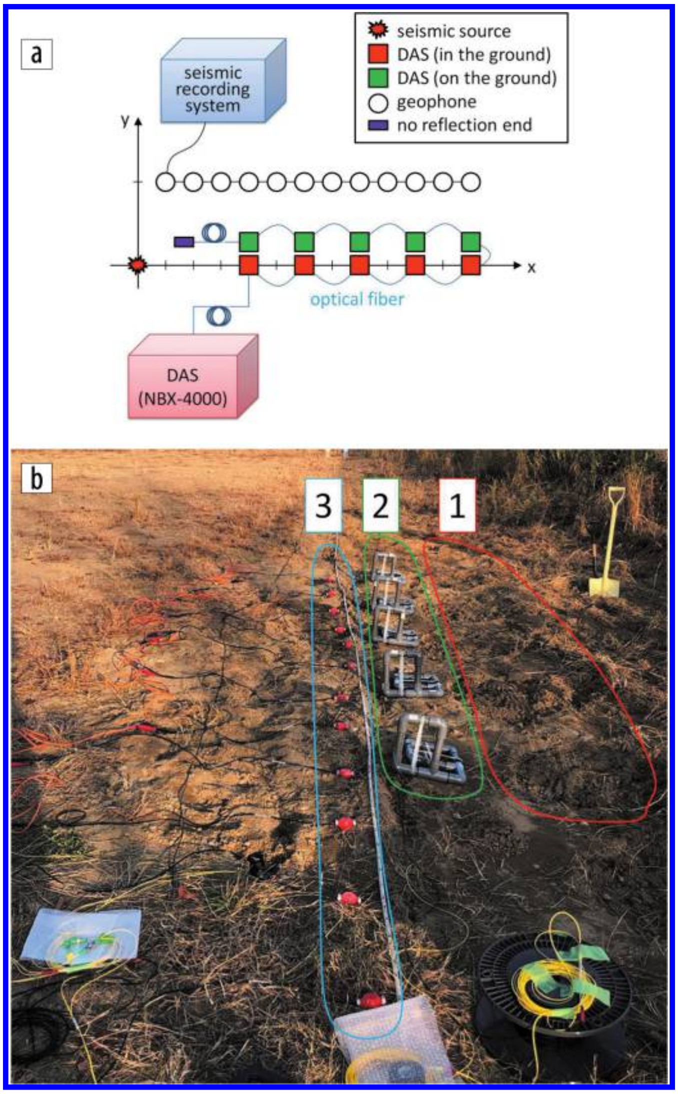

Figure 2. (a) Experimental settings at the test site. The seismic source is located at the origin. Tick marks on *x*- and *y*-axes are set every 0.5 m. The *x*-*y* plane represents the horizontal plane. (b) A photo of the test site after deploying DAS sensors and geophones. 1, 2, and 3 represent DAS sensors in the ground, DAS sensors on the ground, and geophones.

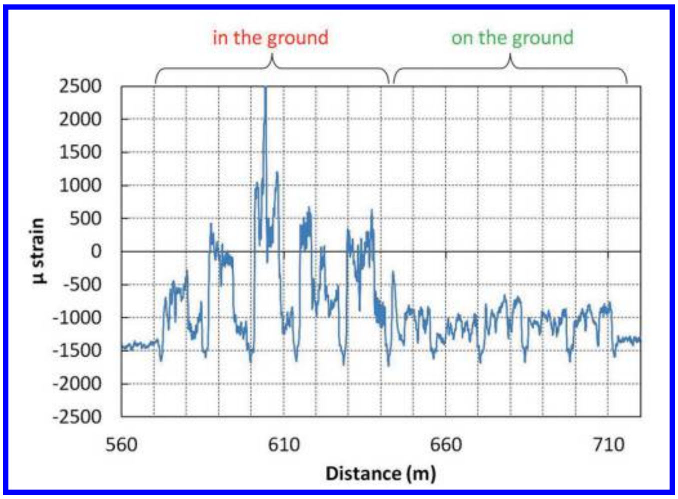

Figure 3. Static strain distribution along the optical fiber measured by BOTDR. The horizontal axis represents the distance from the DAS interrogator, and the vertical axis is in relative static strain.

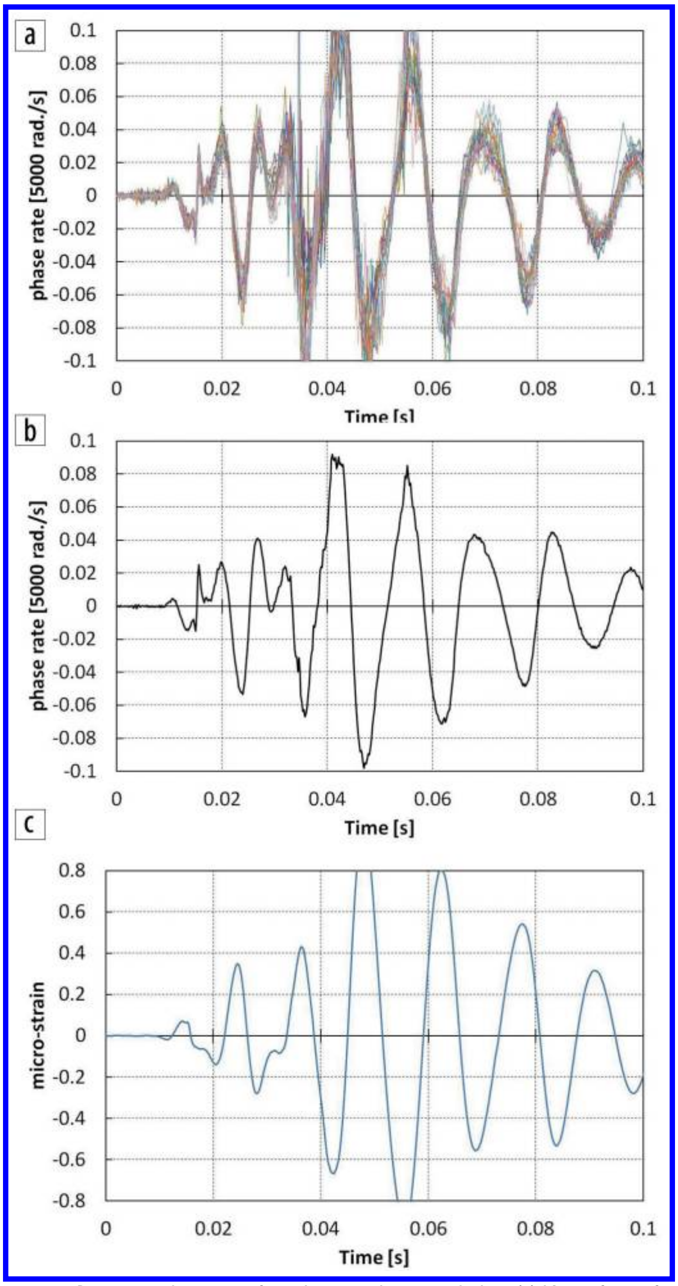

Figure 4. Data conversion process from phase rate data to strain data: (a) 14 waveforms of phase rate, (b) averaging the 14 waveforms, and (c) strain data obtained by integration and conversion.

Before measuring seismic waves, the static strain distribution along the optical fiber was measured by Brillouin optical time-domain reflectometry (BOTDR), as shown in Figure 3. The spatial resolution in this measurement is 0.2 m, which is comparable with the gauge length of the DAS measurement. We observed 10 individual parts with higher strain than the other part. Because the optical fiber was wound around the frame under a constant tensile force, we can recognize the sensor positions on the optical fiber. The five buried sensors have larger strain because of additional overburden pressure. We extracted each sensor location based on the static strain distribution. We also checked that optical power loss is low enough for conducting accurate DAS measurements.

Seismic records

We briefly explain the data processing to obtain the strain data as a function of time. The phase rate data (phase difference at each time step) is obtained by decoding raw data of DAS measurements. Subsequently, we take the average of the phase rate data at the free part of the fiber. The time variation of the phase data is calculated by integrating the phase rate in time. A linear trend (drift) can be seen for some traces after integration. We apply a high-pass filter to the phase data to remove it. Finally, we convert the phase data into the time series of the strain data (seismic records). Figure 4 shows the data conversion at each step.

Figure 5 shows recorded seismic data using the DAS sensor prototypes and geophones. Clear first breaks can be observed in all records. The five DAS sensor prototypes on the ground show strong periodic vibration just after the first-break arrival. Furthermore, a damped oscillation continuing for approximately 1 s can be observed. (The result will be shown in the following section and Figure 11.) In the rest of this section, we focus on the observed records of the five buried DAS sensor prototypes. We read the traveltimes of the first breaks as shown in Figure 6a. The trend of traveltimes in the Y- and Z-components agreed with that of the geophones, whereas the traveltime in the X-component was too large compared with other traveltimes. Because the first breaks are given by P-wave propagation, the aforementioned result means that the X-component had a low sensitivity to P-wave arrival in our experiment. The reason for this insensitivity is discussed in the following section. From the moveout in the traveltimes, the P-wave velocity structure in the test site was

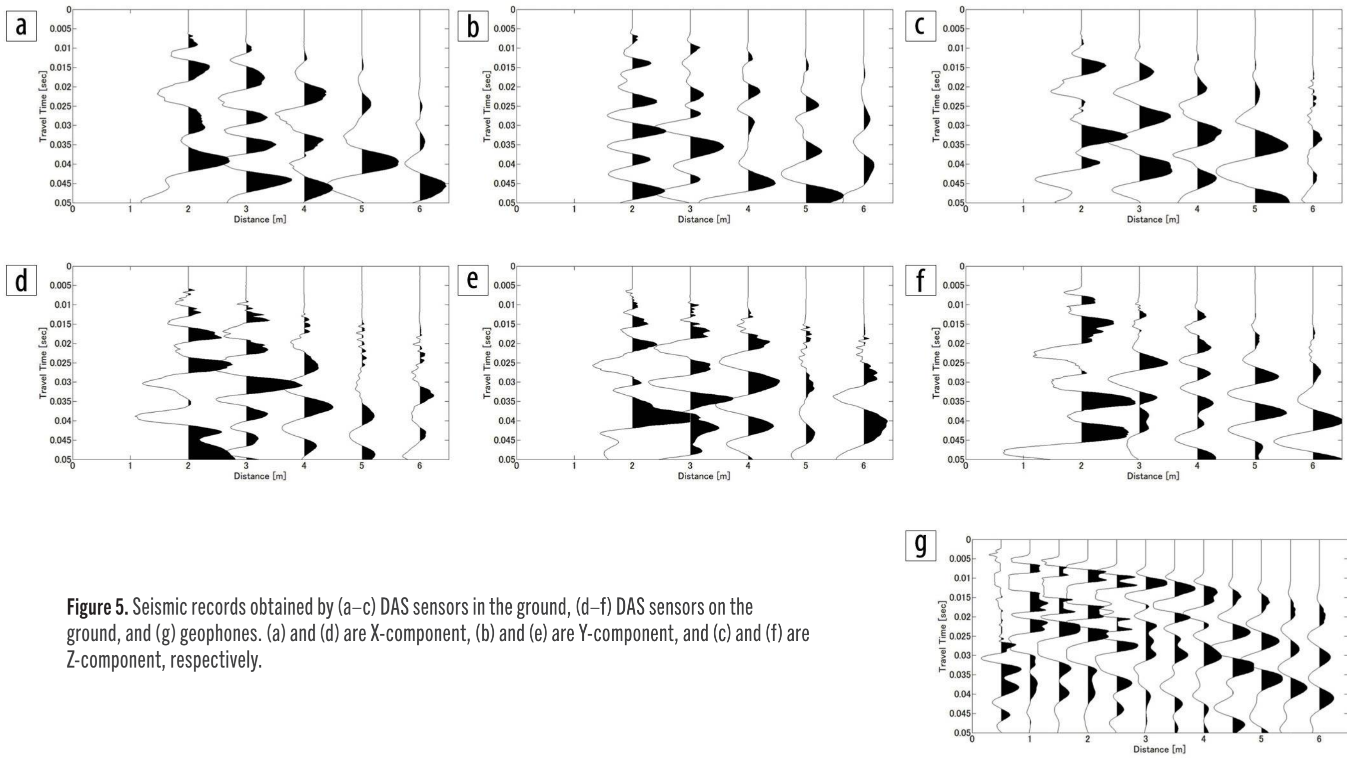

Figure 5. Seismic records obtained by (a–c) DAS sensors in the ground, (d–f) DAS sensors on the ground, and (g) geophones. (a) and (d) are X-component, (b) and (e) are Y-component, and (c) and (f) are Z-component, respectively.

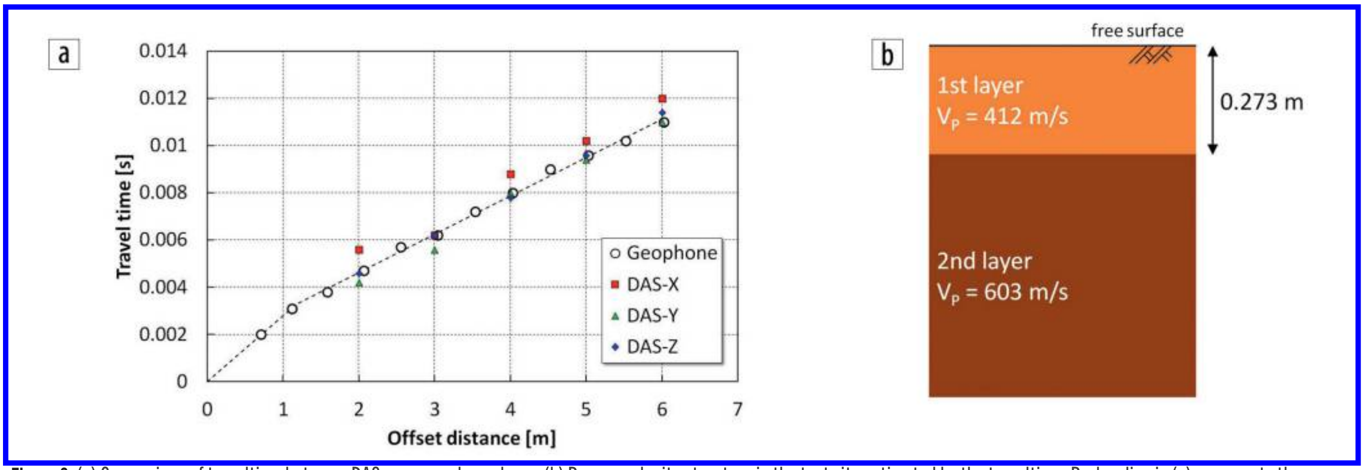

Figure 6. (a) Comparison of traveltime between DAS sensor and geophone. (b) P-wave velocity structure in the test site estimated by the traveltime. Broken line in (a) represents the theoretical traveltime based on the estimated velocity model in (b).

estimated as shown in Figure 6b. We assume a two-layered horizontal structure. The theoretical traveltime curve based on the estimated velocity structure is shown in Figure 6a as a broken line. When we dug the pits for burying the DAS sensor prototypes, the more rigid layer was confirmed at approximately 30 cm depth. The estimated velocity structure agreed with this observation. We also drew the dispersion curves using geophone data (Park et al., 1998), as shown in Figure 7. Although the entire dispersion properties were not so apparent due to the limitation of offset coverage, the fundamental mode at frequencies ranging from 30 to 80 Hz was distinguishable. It can be observed that the fundamental mode of the Rayleigh wave had a phase velocity of about 200–250 m/s at this frequency range.

We compared the obtained seismic waveforms between the DAS sensor prototypes and geophones, shown in Figure 8, for the waveforms acquired at offset distances from 3 to 6 m and 2.5 to 6 m for DAS sensor prototypes and geophones, respectively. The waveforms acquired by the Y-component of the DAS sensor prototype are shown. The waveforms from the two types of sensors at the same locations agree well with each other in early traveltime, especially around the first break. In the later phase, both waveforms have large differences: the recorded amplitudes of geophone waveforms decay quickly in time, whereas the oscillations obtained by the DAS sensor prototypes tail longer. The feature for this difference is also discussed in the following section. Because the geophones used in this study record the vertical motion, seismic data recorded by the Y-component of the DAS sensor prototype correspond to the vertical movement of the ground.

Figure 9 shows the particle motion of the DAS sensor prototype at the offset distances of 3, 4, and 5 m. The vertical and horizontal directions correspond to Y- and Z-components, respectively. At the early arrival time, the oscillating direction shows a rectilinear pattern, whereas, at the later arrival time, the trend of the oscillation changes into circular or ellipsoidal motion. The incidence of body waves generates the early phase with rectilinear motion. On the other hand, the later phase corresponds to the Rayleigh wave, the vibratory track of which is ellipsoidal. Open circles in each trajectory show origination of the ellipsoidal motion. The traveltimes of the origination of the ellipsoidal motion at each sensor are 12.4, 17.8, and 20.6 ms, respectively. Then, the

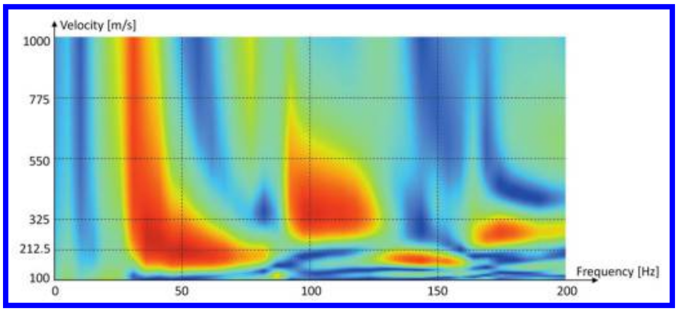

Figure 7. Dispersion curve calculated by geophone data. The horizontal axis is frequency, and the vertical axis is phase velocity.

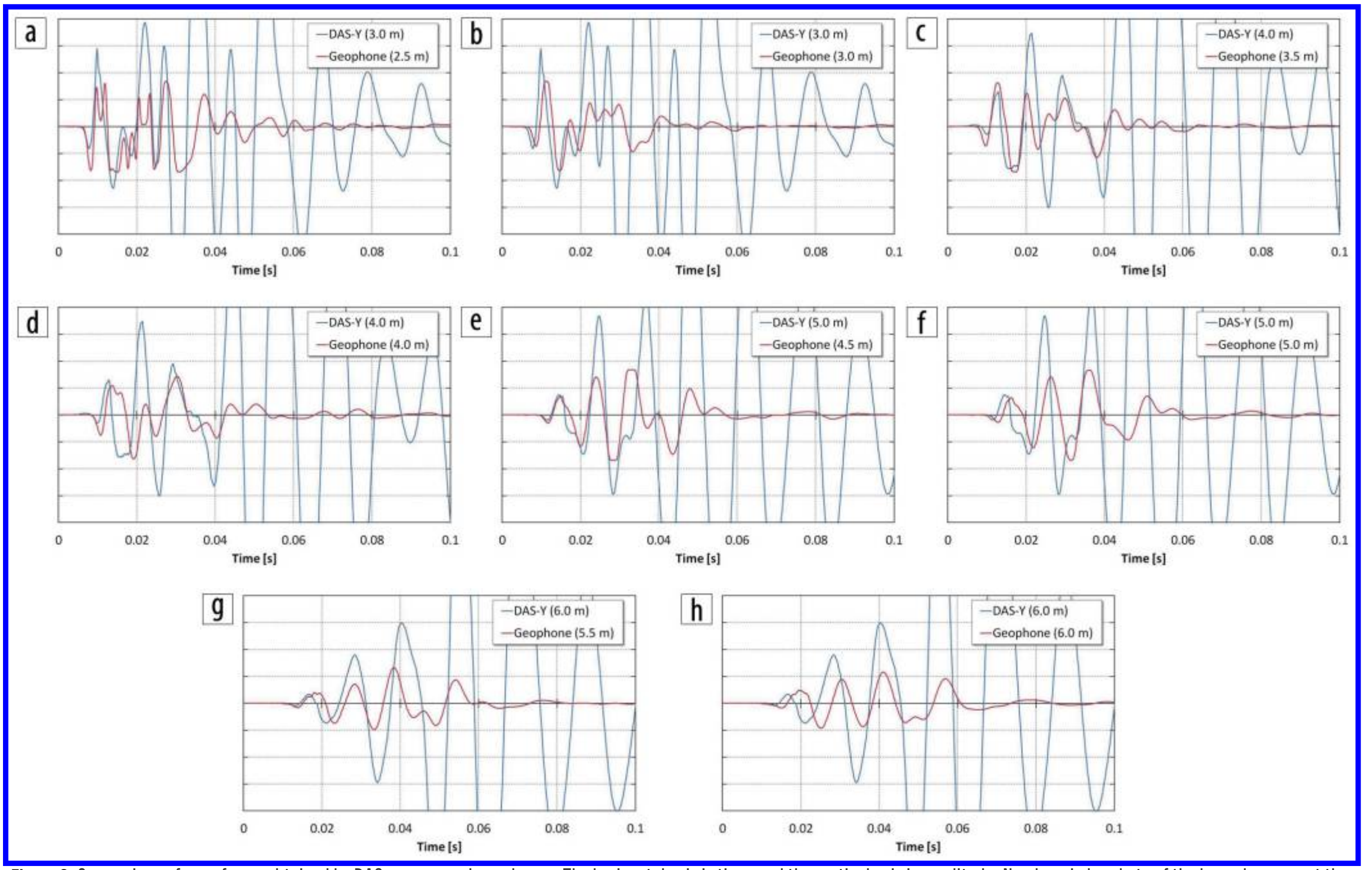

Figure 8. Comparison of waveforms obtained by DAS sensors and geophones. The horizontal axis is time, and the vertical axis is amplitude. Numbers in brackets of the legend represent the *x*-coordinate of sensors.

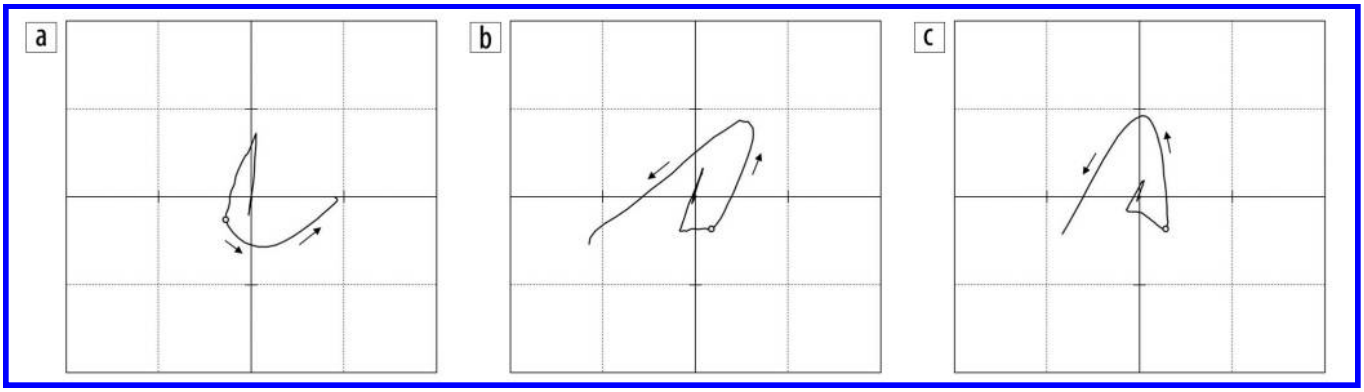

Figure 9. Particle motion of DAS sensor at the offset distances of (a) 3.0 m, (b) 4.0 m, and (c) 5.0 m. The horizontal and vertical directions represent Z- and Y-components, respectively. Open circles on the trajectory indicate the origin points of the ellipsoidal motion.

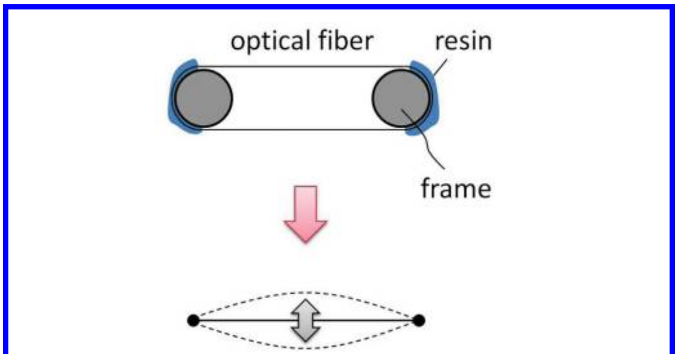

Figure 10. A cross section of the DAS sensor and a string model that explains the recording mechanism of the developed DAS sensor.

propagating velocities can be calculated as 242, 225, and 243 m/s, which have good agreement with the phase velocity of the Rayleigh wave at 30–80 Hz shown in the dispersion curve (Figure 7). Furthermore, the rotating direction shows a coherent trend between each sensor. This result indicates that our DAS sensor prototypes could record the vertical and horizontal ground motions at the same location.

In our observation results, the following remarks are obtained.

- X-component is relatively insensitive to the first break (P-wave arrival) compared to Y- and Z-components.
- Y-component records the vertical motion.
- The ellipsoidal motion can be observed when the particle motion is drawn by taking Y- and Z-components as the vertical and horizontal motions, respectively.
- All components have a longer duration time of oscillation than geophones.

In conclusion, the seismic data recorded by our DAS sensor prototype can be explained by considering a vibration of a string. We make a simple string model and demonstrate the vibration behavior. We try to explain the above remarks by using the string model in the subsequent section.

Analysis based on a string model

We consider a simple string vibration model to examine the recorded seismic data, as shown in Figure 10. The length of the string is l, the applied tensile force to the string is f_T, the line density of the string is ρ, Young's modulus of the string is E, and the cross-sectional area is A. Table 1 shows input values for these parameters. The tensile test measures Young's modulus of the fiber. Because we use the weight of about 100 g for applying the tensile force to the string, f_T is set to 0.98 N. As shown in Figure 11, seismic records obtained by DAS sensor prototypes put on the ground show a damped vibration with a longer duration than the buried one. This result indicates that the interaction between soil and optical fiber affects the damping of vibration. The frequency of oscillation in the later phase (after 0.2 s) is about 60–90 Hz. The natural resonance frequencies of lateral and longitudinal vibrations are calculated as follows:

Table 1. Parameters of the string model.

Parameter	Setting value
Length [m]	0.25
Tensile force [N]	0.98
Line density [kg/m]	0.000776
Young's modulus [GPa]	1.70
Cross-sectional area [mm^2]	0.622

$$f_{\mathrm{lat}} = \frac{1}{2l}\sqrt{\frac{f_T}{\rho}}, \tag{1}$$

$$f_{\mathrm{lon}} = \frac{1}{2l}\sqrt{\frac{EA}{\rho}}, \tag{2}$$

where f_{lat} and f_{lon} are the natural resonance frequencies of lateral and longitudinal vibrations, respectively. For the parameters shown in Table 1, they are calculated as 71 and 2335 Hz, respectively. Therefore, the developed DAS sensor prototypes may record propagating waves as lateral vibration. P-wave propagation generates a displacement field parallel to the direction of the wave propagation. The X-component receives P-waves as longitudinal deformation, whereas Y- and Z-components record them as lateral vibration of the string. Because the rigidity of the optical fiber is relatively high, X-component is not sensitive to P-wave arrival in our experimental configuration. Z-component mainly records the horizontal motion because it is deployed in the vertical direction. This perception would explain why our sensor's particle motion shows ellipsoidal motion.

To further investigate the dynamic response of the string, we conduct numerical experiments with a one-dimensional string model (Uno, 2022). The numerical model is shown in Figure 12a. The string is divided into segments. The mass of each segment is determined by the line density. The motion of the equation is shown as follows:

$$\rho \frac{\partial^2 \mathbf{u}}{\partial t^2} = \mathbf{f}_\mathrm{d} + \mathbf{f}_\mathrm{h} + \mathbf{f}_\mathrm{T}, \tag{3}$$

where $\mathbf{u} = (u_\xi, u_\zeta)^\mathrm{T}$ is the displacement vector; ξ and ζ are local coordinates as shown in Figure 12a; and $\mathbf{f}_\mathrm{d}$, $\mathbf{f}_\mathrm{h}$, and $\mathbf{f}_\mathrm{T}$ are the force vectors due to elastic deformation, attenuation, and initial tensile force, respectively. $\mathbf{f}_\mathrm{d}$ is calculated by the relative displacement between neighboring segments. $\mathbf{f}_\mathrm{h}$ is calculated by the relative velocity with the attenuation coefficient h. As a boundary condition, the forced vibration is applied to both ends; i.e., the displacement field induced by the incident seismic wave is added to both ends. The strain is calculated by the relative displacement between neighboring segments. The output strain of the string is the summation of the strain of each segment. The attenuation coefficient h is a parameter in the numerical experiment. Because the DAS sensor prototypes in the ground have a shorter duration time than those on the ground, a coupling effect between the fiber and surrounding soil would contribute to the attenuation of vibration. Furthermore, a finite duration time of the DAS sensor prototypes on the ground means that the interaction between the fiber and the frame also influences the attenuating behavior. In the present study, we simply introduce the effect of attenuation in a phenomenological manner; i.e., each mechanism of attenuation is not considered directly.

First, we investigate the frequency response of the string. The incident seismic wavefield is assumed to be a monochromatic wavefield. Therefore, both ends vibrate at a regular interval. Figures 12b–12e show the frequency response for different incident angles. The strain is extracted after reaching a steady state. For the parallel incidence ($\theta = 0°$), the induced strain is quite small. On the other hand, a relatively large strain is induced by incident angles of 30°, 60°, and 90°. We can see the peaks of the response at the natural resonance frequency and whole-number multiples of it. This result agrees well with a relatively weak response of the X-component to the first break. Furthermore, it is confirmed that the resonant modes can be reproduced by the simple numerical model.

Next, we apply the displacement recorded by a geophone as the forced vibration. The observed waveform at the offset distance of 5 m is used. Figure 12f shows the time series of the strain with the attenuation coefficient h of 0.5. The time response of strain has a similar trend to the displacement velocity. Figure 12g compares the calculated strain response and DAS data at the offset distance of 5 m. The waveforms at early arrival times have good agreement with each other. The duration times of the ringing effects are also similar to each other. These results agree well with the remarks in the field experimental results. Figure 12h shows the result with a significant attenuation coefficient ($h = 100$). The obtained strain has good agreement with the input displacement. These results indicate that the recorded data may be contaminated by the ringing effect if the attenuation is insufficient. Therefore, for high-quality data, removal of the ringing effect is essential.

Discussion

In the previous section, we investigated the dynamic response of the developed DAS sensor prototype using the string model. The model can basically explain the behavior of optical fiber and observed results. The present DAS sensor prototype may need further improvement for industrial applications. The most important task is to remove the ringing effect of the string from the seismic records. By comparing the data recorded with sensors on the ground to that of buried ones, the oscillatory motion can be suppressed by backfilled soil. However, the duration time of vibration of the buried sensors is still longer than the geophone data. If the damping effect can be controlled more precisely, the seismic response of the DAS sensor prototype would have more similarity to that of the geophone. The other way to remove the ringing effect is appropriate data processing after recording the seismic data with the ringing effect. In this case, all attenuation mechanisms should be modeled precisely.

It also should be noted that the present DAS sensor prototype is designed to act as a point-sensor. In general, DAS measurement obtains the strain (or strain rate) at each point along with the optical fiber. In this field experiment, the gauge length is 0.2 m. To improve S/N, we take an average over 14 waveforms. Then,

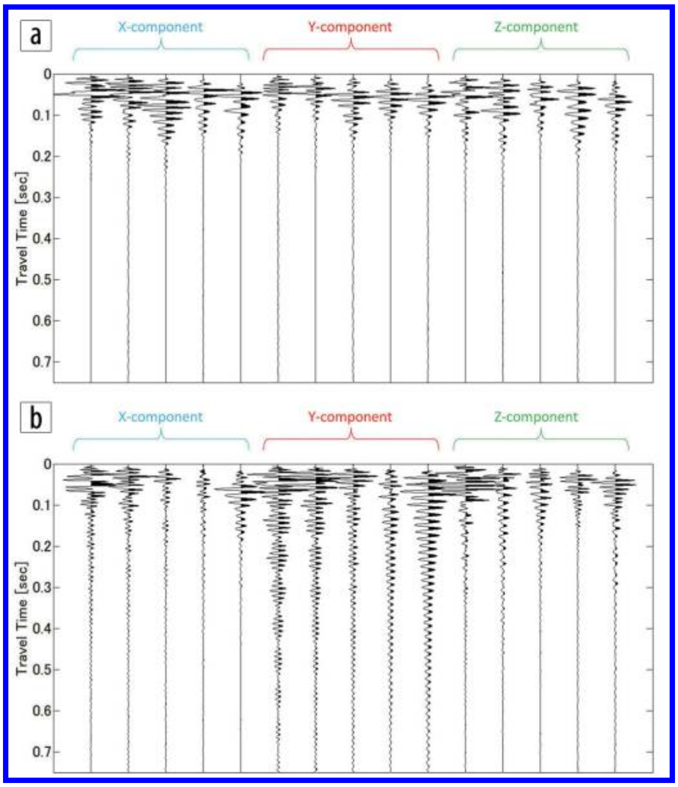

Figure 11. Waveforms recorded by DAS sensors (a) in the ground and (b) on the ground.

the spatial resolution (channel spacing) is 2.8 m if we deploy the optical fiber in a straight line. Because our sensor is deployed at a distance of 1 m, the channel spacing is denser. The minimum spatial resolution of the TGD-OFDR method is 1.8 m (Kishida et al., 2021), but it is still longer than the channel spacing of the present study. Besides, the coupling between the optical fiber and the ground could be a challenging task in the straight deployment. Although the distributed nature is not fully exerted, other advantages (low cost, operation without electric supply) can be utilized. So we believe that the results in this study could be leveraged in various ways in the geophysics society.

Conclusions

In the present study, we developed a new type of DAS sensor prototype. Seismic records were obtained by a prototype of the DAS sensor prototype at a test site. Three individual parts of the sensor record seismic waves in the vertical and horizontal directions. The comparison of the observed data obtained by the DAS sensor prototypes with the geophones indicated that the Y-component of the sensor records the vertical motion of the ground. The particle motion analysis showed that ellipsoidal particle motion, a feature of the Rayleigh wave, could be observed. The propagating velocity of the ellipsoidal motion also agrees well with the phase velocity of the Rayleigh wave estimated by the dispersion property obtained from geophone data. This result indicates that the Z-component of the sensor records the horizontal motion of the ground. The first breaks obtained by Y- and Z-components are consistent with those of the geophone array, whereas the X-component is less sensitive to the first break (P-wave arrival) than the Y- and Z-components. We found that these observations can be explained by analyzing the string vibration. The natural resonance frequency of lateral vibration has good agreement with the observed data. The numerical experiment using the string model also shows the same trend. Therefore, our DAS sensor prototype records seismic waves by the lateral vibration rather than the longitudinal vibration.

The present study shows a new possibility for multicomponent DAS sensors. In our DAS sensor, the frequency response can be easily obtained by a well-known physics problem, i.e., the vibration of a string. In the full-waveform inversion, the frequency response of the sensors must be known for obtaining successful inversion results. Our sensor shows longer continuing oscillation than a geophone. Incorporating a damping mechanism into the sensor would improve the response properties. TLE

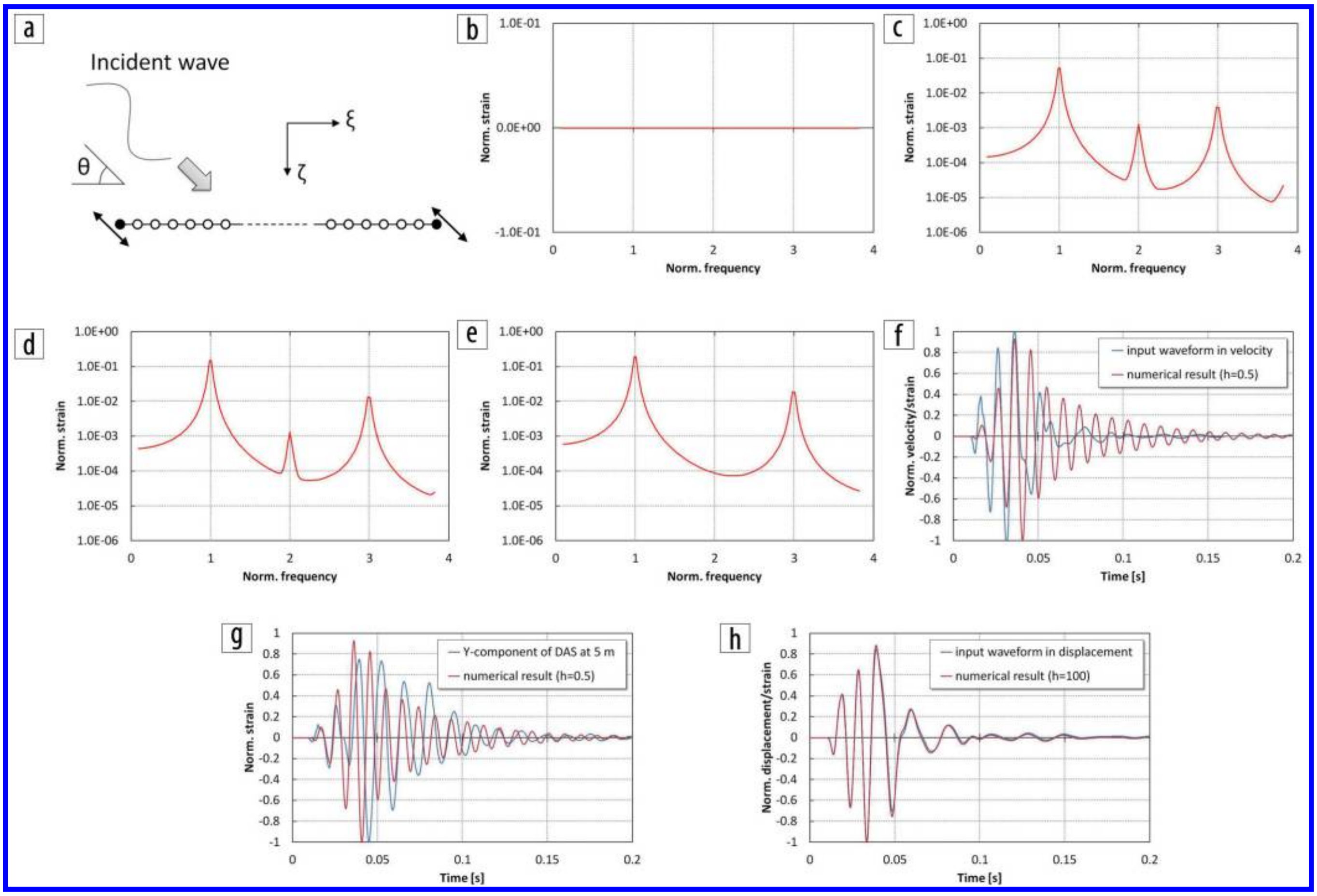

Figure 12. Numerical experimental model and numerical results. (a) Schematic figure of the numerical model. ξ and ζ are local coordinates parallel and perpendicular to the string axis, respectively. Open circles are segment nodes with two degrees of freedom, displacement in ξ and ζ directions. (b–e) The frequency response of the string with the incident angles of 0°, 30°, 60°, and 90°, respectively. The horizontal axis is the frequency normalized by the resonance frequency. The vertical axis is a normalized strain. (f) Comparison between input waveform in velocity and numerical result with the attenuation coefficient of 0.5. (g) Comparison between DAS data of Y-component at the offset distance of 5 m and numerical result with the attenuation coefficient of 0.5. (h) Comparison between input waveform in displacement and numerical result with the attenuation coefficient of 100.

Acknowledgments

We thank associate editor Fabio Tosti, Kris Innanen, and four anonymous reviewers for their thoughtful comments and suggestions, which improved our manuscript significantly. We also thank Pairan Lin, Yusuke Watanabe, Ziyang Zhou, Ryo Masumura, Iktae Jang, Rundong Pan, Kosuke Kayama, Toshiki Matsuo, and Ayane Ishizuki for their support in making the DAS sensors and conducting the field experiment.

Data and materials availability

Data associated with this research are confidential and cannot be released.

Corresponding author: takekawa@tansa.kumst.kyoto-u.ac.jp

References

Bakulin, A., I. Silvestrov, and R. Pevzner, 2020, Surface seismics with DAS: An emerging alternative to modern point-sensor acquisition: The Leading Edge, **39**, no. 11, 808–818, https://doi.org/10.1190/tle39110808.1.

Dou, S., N. Lindsey, A. M. Wagner, T. M. Daley, B. Freifeld, M. Robertson, J. Peterson, C. Ulrich, E. R. Martin, and J. B. Ajo-Franklin, 2017, Distributed acoustic sensing for seismic monitoring of the near surface: A traffic-noise interferometry case study: Scientific Reports, **7**, 11620, https://doi.org/10.1038/s41598-017-11986-4.

Eaid, M. V., S. D. Keating, and K. A. Innanen, 2020, Multiparameter seismic elastic full-waveform inversion with combined geophone and shaped fiber-optic cable data: Geophysics, **85**, no. 6, R537–R552, https://doi.org/10.1190/geo2020-0170.1.

Egorov, A., J. Correa, A. Bóna, R. Pevzner, K. Tertyshnikov, S. Glubokovskikh, V. Puzyrev, and B. Gurevich, 2018, Elastic full-waveform inversion of vertical seismic profile data acquired with distributed acoustic sensors: Geophysics, **83**, no. 3, R273–R281, https://doi.org/10.1190/geo2017-0718.1.

Hartog, A., B. Frignet, D. Mackie, and M. Clark, 2014, Vertical seismic optical profiling on wireline logging cable: Geophysical Prospecting, **62**, no. 4, 693–701, https://doi.org/10.1111/1365-2478.12141.

Hornman, K., B. Kuvshinov, P. Zwartjes, and A. Franzen, 2013, Field trial of a broadside-sensitive distributed acoustic sensing cable for surface seismic: 75th Conference and Exhibition, EAGE, Extended Abstracts, https://doi.org/10.3997/2214-4609.20130383.

Hornman, J. C., 2017, Field trial of seismic recording using distributed acoustic sensing with broadside sensitive fibre-optic cables: Geophysical Prospecting, **65**, no. 1, 35–46,https://doi.org/10.1111/1365-2478.12358.

Innanen, K. A., D. Lawton, K. Hall, K. L. Bertram, M. B. Bertram, and H. C. Bland, 2019, Design and deployment of a prototype multicomponent distributed acoustic sensing loop array: 89th Annual International Meeting, SEG, Expanded Abstracts, 953–957, https://doi.org/10.1190/segam2019-3216304.1.

Kimura, T., K. Suzuki, S. Ali, J. Breninger, J. Tessman, I. Z. Mahmoud, and S. Hajjaj, 2018, Hybrid 3D VSP using fiber-optic technology and a conventional borehole seismic array tool: 80th Conference and Exhibition, EAGE, Extended Abstracts, https://doi.org/10.3997/2214-4609.201801499.

Kishida, K., A. Guzik, K. Nishiguchi, T. Li, D. Azuma, Q. Liu, and Z. He, 2020, Commercialization of real-time distributed acoustic fiber optic sensing (DAS) utilizing chirped pulse: IEICE Technical Report, 120, 39–44.

Kishida, K., A. Guzik, K. Nishiguchi, C.-H. Li, D. Azuma, Q. Liu, and Z. He, 2021, Development of real-time time gated digital (TGD) OFDR method and its performance verification: Sensors, **21**, no. 14, 4865, https://doi.org/10.3390/s21144865.

Kuvshinov, B. N., 2016, Interaction of helically wound fibre-optic cables with plane seismic waves: Geophysical Prospecting, **64**, no. 3, 671–688, https://doi.org/10.1111/1365-2478.12303.

Lindsey, N. J., T. C. Dawe, and J. B. Ajo-Franklin, 2019, Illuminating seafloor faults and ocean dynamics with dark fiber distributed acoustic sensing: Science, **366**, no. 6469, 1103–1107, https://doi.org/10.1126/science.aay5881.

Luo, B., W. Trainor-Guitton, E. Bozdag, L. LaFlame, S. Cole, and M. Karrenbach, 2020, Horizontally orthogonal distributed acoustic sensing array for earthquake- and ambient-noise-based multichannel analysis of surface waves: Geophysical Journal International, **222**, no. 3, 2147–2161, https://doi.org/10.1093/gji/ggaa293.

Mateeva, A., J. Lopez, J. Mestayer, P. Wills, B. Cox, D. Kiyashchenko, Z. Yang, W. Berlang, R. Detomo, and S. Grandi, 2013, Distributed acoustic sensing for reservoir monitoring with VSP: The Leading Edge, **32**, no. 10, 1278–1283, https://doi.org/10.1190/tle32101278.1.

Ning, I. L. C., and P. Sava, 2018, Multicomponent distributed acoustic sensing: Concept and theory: Geophysics, **83**, no. 2, P1–P8, https://doi.org/10.1190/geo2017-0327.1.

Park, C. B., R. D. Miller, and J. Xia, 1998, Imaging dispersion curves of surface waves on multi-channel record: 68th Annual International Meeting, SEG, Expanded Abstracts, 1377–1380, https://doi.org/10.1190/1.1820161.

Rusmanugroho, H., and G. A. McMechan, 2012, 3D, 9C seismic modeling and inversion of Weyburn field data: Geophysics, **77**, no. 4, R161–R173, https://doi.org/10.1190/geo2011-0406.1.

Spica, Z. J., M. Perton, E. R. Martin, G. C. Beroza, and B. Biondi, 2020, Urban seismic site characterization by fiber-optic seismology: Journal of Geophysical Research: Solid Earth, **125**, no. 3, e2019JB018656, https://doi.org/10.1029/2019JB018656.

Takekawa, J., H. Mikada, S. Xu, M. Uno, P. Lin, Y. Watanabe, Z. Zhou, et al., 2021, Fundamental study of a multiple component DAS sensor: Sixth International Conference on Engineering Geophysics, SEG, Expanded Abstracts, 311–315, https://doi.org/10.1190/iceg2021-079.1.

Uno, M., 2022, Dynamic response analysis of optical fiber in DAS sensor for near surface seismic survey: B.S. thesis, Kyoto University.

Watanabe, Y., H. Mikada, and J. Takekawa, 2017, Estimate azimuthal shear-wave anisotropy by applying virtual-source method with a line of air-gun shots and a single ocean-bottom seismometer: 87th Annual International Meeting, SEG, Expanded Abstracts, 2476–2480, https://doi.org/10.1190/segam2017-17666236.1.